

Cite this: *J. Mater. Chem. C*, 2018, **6**, 4936

The optimized growth of AlN templates for back-illuminated AlGaIn-based solar-blind ultraviolet photodetectors by MOCVD

Yiren Chen,[†] Zhiwei Zhang,[†] Hong Jiang,* Zhiming Li,[†] Guoqing Miao and Hang Song*

In this paper, AlN templates with different mesothermal AlN (MT-AlN) interlayer deposition cycles are prepared via metal-organic chemical vapor deposition (MOCVD) at first. The influence of the MT-AlN interlayer on the crystalline quality of AlN templates has been carefully investigated. The results show that the MT-AlN interlayer played the role of providing a strain gradient to release the strain from AlN along the growth direction. The crystalline quality, surface morphology and residual compressive stress of AlN templates can be greatly optimized through introducing one MT-AlN interlayer cycle during the growth of HT-AlN. And then, a PIN structure back-illuminated AlGaIn-based solar-blind ultraviolet photodetector (SUV-PD) is further designed, grown and fabricated based on the optimized AlN template. The SUV-PD exhibits a low dark current density, a bandpass spectral responsivity with a peak value of 0.15 A W^{-1} at 271 nm, corresponding to an EQE as high as 68.8%, and a response speed of 6.5 ns. These results strongly reflect the high quality of AlN templates prepared via inserting a MT-AlN interlayer based on a common growth method.

Received 11th February 2018,
Accepted 13th April 2018

DOI: 10.1039/c8tc00755a

rsc.li/materials-c

1. Introduction

As part of the third generation of semiconductors, GaN-based materials have achieved great success in the field of optoelectronics, mainly in relation to light-emitting diodes (LEDs)^{1–3} and laser diodes (LDs).^{4,5} In recent years, because of its wide direct and tunable band gap (with its corresponding spectrum covering from 200 nm to 365 nm), fully solid-state, filter-free nature, and potential application to missile warning and guidance, flame monitoring and early detection, free-space confidential optical communication, ozone layer monitoring, and chemical/biological agent sensing,⁶ there is growing interest in solar-blind ultraviolet photodetectors (SUV-PDs) based on the ternary alloy material AlGaIn. The development of high-performance AlGaIn-based SUV-PDs is expected to provide a promising alternative, instead of conventional photomultiplier tubes (PMTs) or Si-based photodiodes equipped with a complex and costly deep ultraviolet band-pass filter.⁷ However, unfortunately, the performance of AlGaIn-based SUV-PDs is severely restricted by the crystalline quality of high Al-content AlGaIn at the present time. This is because, until now, the preparation of high Al-content AlGaIn has mainly been performed using AlN layers due to the lack of

homogeneous substrates. An AlN single crystal is always considered to be an ideal substrate for the growth of AlGaIn material due to its high crystalline quality, direct wide band gap and excellent lattice matching with GaN.^{8,9} However, under existing mainstream growth methods, including solution growth^{10,11} and sublimation-recondensation,¹² the application of bulk AlN substrate is greatly limited by size and price up to now. The heteroepitaxial growth of AlN on a lattice-mismatched sapphire substrate (a so-called AlN template) via metal-organic chemical vapor deposition (MOCVD), hydride vapor phase epitaxy (HVPE) or molecular beam epitaxy (MBE) has been thus developed and extensively adopted as an alternative. The crystalline quality of the AlN template will directly determine that of high Al-content AlGaIn. Unfortunately, the large lattice and thermal expansion mismatch between AlN and sapphire, as well as the weak surface migration of aluminum species on sapphire, lead to a high-density of dislocations in the AlN template, which will extend to the subsequent high Al-content AlGaIn epitaxial layers. These dislocations will act as nonradiative recombination centers or leakage passages in AlGaIn-based optoelectronic devices, and thus restrict their performance.^{13,14} Therefore, the preparation of high-quality AlN on sapphire is of great significance to realize high-efficiency AlGaIn-based optoelectronic devices. In the past decade, a series of methods, including the use of low temperature interlayers,¹⁵ alternating high and low V/III ratio AlN,¹⁶ epitaxial lateral overgrowth on nanopatterned substrates,¹⁷ AlN/AlGaIn superlattice interlayers,¹⁸ NH₃ nitridation,¹⁹ pulsed atomic layer

State Key Laboratory of Luminescence and Applications,
Changchun Institute of Optics, Fine Mechanics and Physics,
Chinese Academy of Sciences, Changchun 130033, People's Republic of China.
E-mail: jiangh@ciomp.ac.cn, songh@ciomp.ac.cn

[†] These authors contributed equally.

epitaxy (PALE) techniques,²⁰ and high-temperature annealing,^{21,22} have been proposed to improve the crystalline quality of AlN templates.

In this work, we present our study on the optimized growth of AlN templates *via* MOCVD at first. The method of introducing a mesothermal AlN (MT-AlN) interlayer on the basis of a traditional two-step growth method was adopted. The effects of different MT-AlN interlayer cycles on the crystalline quality of AlN templates were investigated in detail. Then, a type of AlGaN-based solar-blind ultraviolet photodetector was designed and grown on the optimized AlN template, and finally, the performance of the back-illuminated AlGaN-based SUV-PD was carefully evaluated to reflect the high quality of the AlN template.

2. Experimental

2.1 MOCVD growth of AlN templates

The AlN templates were grown on 2 inch single polished *c*-plane sapphire substrates *via* low-pressure MOCVD. Trimethylaluminum (TMAl) and ammonia (NH₃) were used as Al and N precursors, respectively. Hydrogen (H₂) was used as the carrier gas. The growth conditions for the AlN templates are listed in Table 1, and corresponding *in situ* monitoring curves *vs.* time recorded during the growth process are presented in Fig. 1. Prior to growth, all of the sapphire substrates were thermally desorbed at 1100 °C under H₂ for 480 s. Sample A was grown using a conventional two-step method, with a 35 nm-thick low-temperature AlN (LT-AlN) nucleation layer and a 1 μm-thick high-temperature AlN (HT-AlN) epilayer. For sample B, in addition to a 35 nm-thick LT-AlN nucleation layer and a 200 nm-thick HT-AlN epilayer, one 60 nm-thick MT-AlN interlayer and one 750 nm-thick HT-AlN epilayer cycle were undergone subsequently. In comparison to sample B, sample C used two 60 nm-thick MT-AlN interlayer and two 350 nm-thick HT-AlN epilayer cycles, while sample D used three 60 nm-thick MT-AlN and three 210 nm-thick HT-AlN epilayer cycles. In the growth process, all of the LT-AlN nucleation layers were grown at 950 °C with a V/III ratio of about 2000 and a reactor pressure of 50 mbar. Also, all of the MT-AlN interlayers were grown at 1050 °C with a V/III ratio of about 700 and a reactor pressure of 40 mbar, while all of the HT-AlN epilayers were grown at 1280 °C with a V/III ratio of about 200 and a reactor pressure of 40 mbar.

2.2 MOCVD growth of an AlGaN-based SUV-PD structure on optimized AlN templates

Trimethylaluminum (TMAl), trimethylgallium (TMGa), and ammonia (NH₃) were used as Al, Ga, and N precursors, respectively,

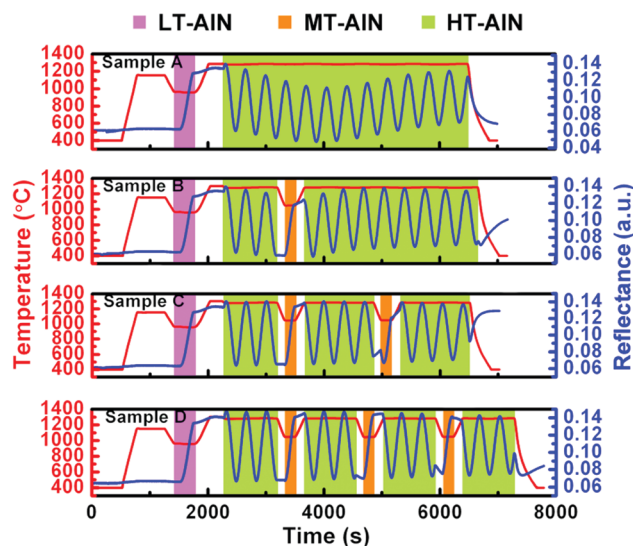


Fig. 1 *In situ* monitoring curves *vs.* time for the AlN templates. The left ordinate is the process temperature and the right ordinate is the short-wavelength (405 nm) reflectance.

while dicyclopentadienyl magnesium (Cp₂Mg) and silane (SiH₄) were used as p- and n-type dopants. Based on an optimized AlN template, an AlGaN-based SUV-PD structure was further grown. The SUV-PD structure was based on a PIN structure, mainly including ten periods of Al_{0.55}Ga_{0.45}N/AlN (6 nm/6 nm) superlattices (SLs) to regulate the stress and suppress dislocation extension from the AlN template,²³ a 200 nm-thick intrinsic Al_{0.55}Ga_{0.45}N (i-Al_{0.55}Ga_{0.45}N) layer, a 450 nm-thick Si-doped Al_{0.55}Ga_{0.45}N (n-Al_{0.55}Ga_{0.45}N) layer, a 60 nm-thick n-AlGa_{0.4}N gradient layer with the Al content gradually changing from 0.55 to 0.46, a 300 nm-thick i-Al_{0.46}Ga_{0.54}N layer, a 80 nm-thick Mg-doped Al_{0.4}Ga_{0.6}N (p-Al_{0.4}Ga_{0.6}N), and a 20 nm-thick p-AlGa_{0.4}N gradient layer with the Al content gradually changing from 0.4 to 0.2 in sequence. The carrier concentrations in the n-Al_{0.55}Ga_{0.45}N and p-Al_{0.4}Ga_{0.6}N layers were about $1.2 \times 10^{18} \text{ cm}^{-3}$ and $2.2 \times 10^{17} \text{ cm}^{-3}$, respectively, which were evaluated based on the epitaxial wafer, *via* an electrochemical capacitance–voltage (ECV) method.

2.3 Characterization

A 405 nm *in situ* optical monitoring system (LayTec AG) was used to obtain the reflectance during the growth process. The AlN templates were also characterized using an atomic force microscope (AFM, Veeco multi-mode) and a high-resolution X-ray diffractometer (HRXRD, Bruker D8), using the rocking curve

Table 1 Growth conditions for the AlN templates

Growth layer	Growth conditions			Sample A		Sample B		Sample C		Sample D	
	Temperature (°C)	V/III ratio	Pressure (mbar)	Thickness (nm)	Period						
LT-AlN	950	2000	50	35	1	35	1	35	1	35	1
HT-AlN	1280	200	40	1010	1	200	1	200	1	200	1
MT-AlN	1050	700	40	None	None	60	1	60	2	60	3
HT-AlN	1280	200	40	None	None	750	1	350	2	210	3

scan and asymmetrical reciprocal space mapping (RSM) around the (10 $\bar{1}$ 5) reflection. Raman scattering spectra from the AlN templates were recorded in backscattering geometry using the 488 nm line of an Ar⁺ ion laser (LabRam Infinity) as the excitation source. A semiconductor parameter analyzer (Agilent B1500A) was used to measure the current–voltage (*I*–*V*) characteristics of the back-illuminated AlGa_xN-based SUV-PD. The spectral responsivity and corresponding external quantum efficiency (EQE) for the AlGa_xN-based SUV-PD were measured using an ultraviolet spectral response test system, which was equipped with a xenon lamp as the light source, a chopper, a monochromator, a lock-in amplifier, and a calibrated UV-enhanced Si-based photodetector as the standard reference. The transient spectral response of the photodetector was stimulated using a 10 mW 266 nm-wavelength Nd:YAG laser and recorded with a digital oscilloscope (Tektronix DPO 5104).

2.4 Device fabrication

After finishing the epitaxial growth of the AlGa_xN-based SUV-PD structure on an optimized AlN template, the wafer was rapidly annealed at 850 °C under an N₂ atmosphere in order to activate the Mg dopants in the p-type material. Subsequently, an inductively-coupled plasma (ICP) etching method was adopted to etch the material to the n-Al_{0.55}Ga_{0.45}N layer, assisted by a standard photolithography process, leaving a 300 μm-diameter mesa-style circle. Then, surrounding the mesa and on top of the mesa, a Ti/Al/Ni/Au (30/100/30/300 nm) ring-like multilayer electrode and a Ni/Au (30/300 nm) circular electrode were respectively deposited *via* electron beam evaporation. Finally, the whole device was rapidly annealed at 700 °C for 60 s under an N₂ atmosphere to realize ohmic contact.

3. Results and discussion

Fig. 1 presents the growth processes and 405 nm *in situ* optical monitoring curves for samples A, B, C, and D. The differences in the four samples with relation to the growth process have been described in detail in the experimental section. It is well known that reflectance oscillation curves can directly reflect the surface roughness of epitaxial films. Generally, increasing surface roughness results in low oscillation intensity or a rapidly damping amplitude.²⁴ In comparison, for sample A, which is grown *via* a traditional two-step method without a MT-AlN interlayer, the reflectance intensity of the 405 nm *in situ* monitoring curve during HT-AlN growth undergoes a process of decreasing and then rising. This is commonly attributed to a transition in the growth mode from three-dimensional (3D) island growth to quasi-two-dimensional (2D) layer-by-layer growth. Apparently, samples B, C, and D, with a MT-AlN interlayer, present steady and uniform reflectance intensity in the 405 nm *in situ* monitoring curve, which results from the introduction of a MT-AlN interlayer that accelerates the transition from 3D island growth to 2D layer-by-layer growth during the HT-AlN growth process. It can be said that, according to the reflectance curves, the surfaces of samples B, C, and D should be smoother than that of sample A.

Fig. 2(a)–(d) shows AFM images of samples A, B, C, and D, respectively, which are used to confirm this viewpoint. The scan

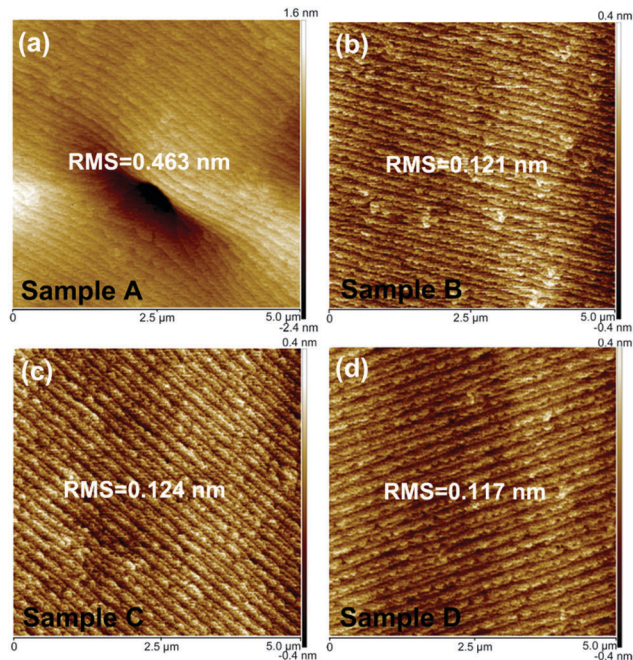


Fig. 2 AFM images of samples A, B, C, and D grown with different MT-AlN interlayer cycles. The scan area of the AFM images is 5 × 5 μm².

area is 5 × 5 μm². As can be seen, the surface morphology of sample A presents poor flatness, due to the existence of V-type defects, although it has atomic steps. Its root mean square (RMS) roughness is 0.463 nm. In contrast, samples B, C, and D, with a MT-AlN interlayer, present flat, crack-free and clear atomic step morphologies without any V-type defects or hillocks. Moreover, their RMS roughness is only about 0.12 nm, which is greatly improved. However, under the same growth conditions, increasing the MT-AlN interlayer cycles has no obvious effect on the surface morphology of the AlN samples, as demonstrated by a comparison of the RMS values of samples B, C, and D.

In order to further understand the influence of the MT-AlN interlayer on the quality of the AlN templates, the full width at half maximum (FWHM) values of the (0002) and (10 $\bar{1}$ 2) planes are demonstrated for the four samples in Fig. 3, which are

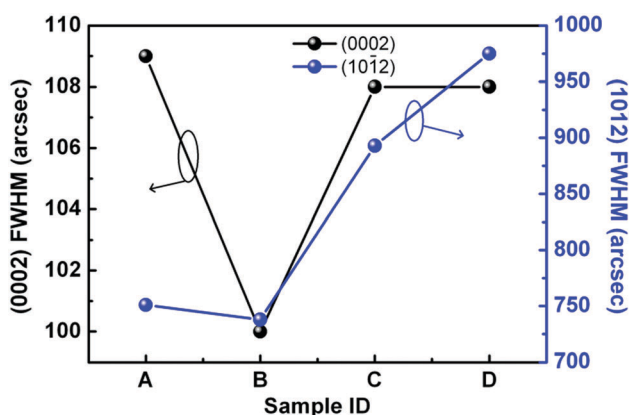


Fig. 3 The FWHM values of the (0002) and (10 $\bar{1}$ 2) planes of samples A, B, C, and D.

calculated from the rocking curves of the (0002) and (10 $\bar{1}2$) planes. The FWHM values of the (0002) plane are 109, 100, 108, and 108 arcsec, while the values of the (10 $\bar{1}2$) plane are 751, 738, 893, and 975 arcsec, corresponding to samples A, B, C and D, respectively. FWHM values are extensively used to evaluate dislocations in AlN films.²⁵ The broadening of the FWHM is mainly related to misorientations of crystallites, which can be described in terms of the out-of-plane tilt and the in-plane twist angle. Depending on the Burgers vector, the tilt and twist misorientations of crystallites are closely associated with screw and edge dislocations, respectively.^{26,27} Thus, in the case of randomly distributed dislocations, the screw dislocation density (ρ_s) and edge dislocation density (ρ_e) can be evaluated *via*^{9,28}

$$\rho_s = \beta_{(0002)}^2 / (2\pi \ln 2 \times |b_c|^2)$$

$$\rho_e = \beta_{(10\bar{1}2)}^2 / (2\pi \ln 2 \times |b_a|^2)$$

where $\beta_{(0002)}$ and $\beta_{(10\bar{1}2)}$ separately denote the FWHM values of the (0002) and (10 $\bar{1}2$) planes, and b_c and b_a stand for the Burgers vector lengths equating to the c - and a -axial lattice constants, respectively. Therefore, ρ_s and ρ_e are calculated to be 2.54×10^7 and $5.48 \times 10^9 \text{ cm}^{-2}$ for sample A, 2.14×10^7 and $5.19 \times 10^9 \text{ cm}^{-2}$ for sample B, 2.51×10^7 and $8.04 \times 10^9 \text{ cm}^{-2}$ for sample C, and 2.52×10^7 and $9.74 \times 10^9 \text{ cm}^{-2}$ for sample D. The results reveal that one MT-AlN interlayer cycle is best to reduce the dislocation density in the AlN template and improve its crystalline quality.

The Raman spectra in Fig. 4 and the asymmetrical RSMs around the (10 $\bar{1}5$) reflection in Fig. 5 are both presented to evaluate stress evolution in samples A, B, C, and D. As shown in Fig. 4(a), excluding the peaks of c -plane sapphire, samples B, C, and D with a MT-AlN interlayer exhibit two other peaks located at frequencies of: 658.95 cm^{-1} and 889.93 cm^{-1} ; 660.49 cm^{-1} and 889.93 cm^{-1} ; and 660.49 cm^{-1} and 892.896 cm^{-1} , respectively. These two peaks correspond to the $E_2(\text{h})$ and $A_1(\text{LO})$ phonon modes, respectively. Distinguishably from samples B, C, and D, an additional peak located at 910.68 cm^{-1} , which is in accordance with the $E_1(\text{LO})$ phonon mode, is measured in sample A, besides the $E_2(\text{h})$ and $A_1(\text{LO})$ phonon modes. Generally, only the $E_2(\text{h})$ and $A_1(\text{LO})$ phonon modes are allowed for the $z(\text{yy})\bar{z}$ scattering configuration at the normal incidence of an excited laser along the c -axis, while the $E_1(\text{LO})$ phonon mode is allowed for the

$y(\text{xz})\bar{x}$ scattering configuration.^{9,29,30} Therefore, the existence of the $E_1(\text{LO})$ phonon mode means there are disoriented crystallites in sample A, which is quite in agreement with the AFM morphology shown in Fig. 2(a). In addition, the frequency shifts of the phonon modes are closely related to the stress in the epitaxial material. It is reported that for nitride semiconductors, the Raman frequency will shift to the higher frequency side of the stress-free position due to the existence of residual compressive stress and to the lower frequency side due to the existence of residual tensile stress.³¹ The frequency shift of $E_2(\text{h})$, which is a main phonon mode of AlN growing along the c -axis, determines its stress state. The phonon frequency of $E_2(\text{h})$ for stress-free AlN is 657.4 cm^{-1} at room-temperature.³² Therefore, as seen in Fig. 4(b), the Raman frequency of the $E_2(\text{h})$ phonon mode for all samples shifts to the higher frequency side of the stress-free position, which indicates the existence of residual compressive stress. Due to the linear relationship between the Raman shift of the $E_2(\text{h})$ phonon mode and the biaxial stress, sample A, grown *via* a traditional two-step growth method, presents the strongest residual compressive stress among the four samples. However, sample B, with one MT-AlN interlayer cycle, presents the weakest residual compressive stress compared to the other samples, on account of the smallest frequency offset of the $E_2(\text{h})$ phonon mode. That is to say, inserting one MT-AlN interlayer cycle during the HT-AlN growth process is beneficial to decrease the residual compressive stress in the AlN template.

In order to further demonstrate the strain evolution in the AlN epilayers in relation to different MT-AlN interlayer cycles, asymmetrical RSMs of four samples are measured around the (10 $\bar{1}5$) reflection, as shown in Fig. 5. A well-resolved main peak and a series of contour lines are presented in each RSM. In Fig. 5, q_x and q_z are in directions parallel and perpendicular to the surface of the AlN epilayer, and can be used to calculate the in-plane and out-of-plane lattice constants *via*^{23,33}

$$a = 2((h^2 + hk + k^2)/(3q_x^2))^{1/2}$$

$$c = l/q_z$$

where h , k , and l are the Miller indices. The lattice constants for unstrained bulk AlN are 0.31127 nm and 0.49817 nm for a_0 and c_0 , respectively.³⁴ Therefore, the reciprocal lattice point (RLP), denoted as (q_x, q_z) for fully relaxed AlN, can be calculated as $(-3.71, 10.037)$ for the (10 $\bar{1}5$) reflection. In contrast, the RLPs of the main peaks for samples A, B, C and D are measured as $(-3.708, 10.036)$, $(-3.709, 10.037)$, $(-3.706, 10.037)$, and $(-3.706, 10.037)$, respectively. These results reveal that the introduction of a MT-AlN interlayer benefits the release of strain along the growth direction. The additional lattice distortion in samples B, C, and D can be inferred from the broadening of the low-intensity RSM component in the growth direction, which can be attributed to the presence of a MT-AlN interlayer, as the strain gradient elongates along the direction perpendicular to the sample surface. Furthermore, no diffuse scattering can be observed around the gradient region, indicating that the change in lattice parameters because of the MT-AlN interlayer is not accompanied by structural defect formation. These are the reasons that samples with a MT-AlN interlayer present flat,

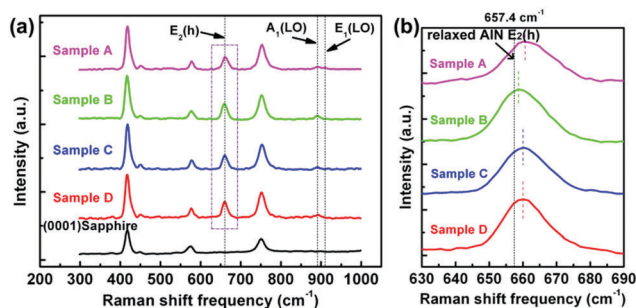


Fig. 4 (a) Raman spectra of samples A, B, C, and D. (b) A partially enlarged image of the Raman spectra, corresponding to the purple dotted box in (a).

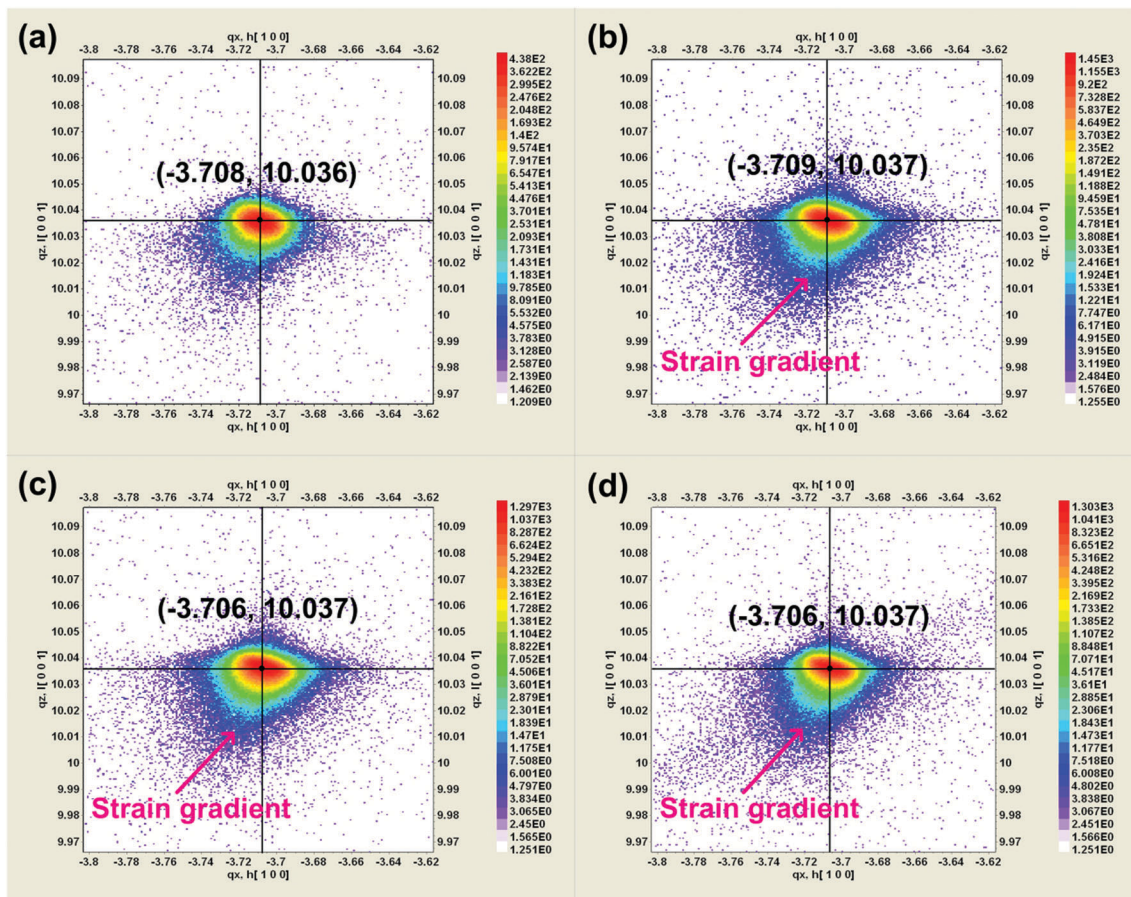


Fig. 5 Asymmetrical RSMs around the $(10\bar{1}5)$ reflection for samples (a) A, (b) B, (c) C, and (d) D.

crack-free and clear atomic step morphologies. Among samples B, C, and D, sample B, with one MT-AlN interlayer cycle, exhibits the largest strain gradient, which means the best strain relief.

Based on the results mentioned above, an optimized AlN template can be obtained by inserting one MT-AlN interlayer cycle. An AlGa_{0.4}N-based SUV-PD structure is designed and grown on the optimized AlN template. Fig. 6(a) shows a schematic diagram of the configuration of the PIN structure back-illuminated AlGa_{0.4}N-based SUV-PD. The growth process is depicted in the experimental section in detail. A typical (0002) plane $2\theta - \omega$ scan curve for the epitaxial wafer is obtained *via* HRXRD. As can be seen in Fig. 6(b), there are five main peaks, located at 35.06° , 35.3° , 35.34° , 35.64° , and 36° , which correspond to the Al_{0.4}Ga_{0.6}N, Al_{0.46}Ga_{0.54}N, Al_{0.55}Ga_{0.45}N, Al_{0.55}Ga_{0.45}N/AlN SL, and AlN layers, respectively, and an AlGa_{0.4}N gradient layer is located to the left of the Al_{0.4}Ga_{0.6}N layer, which is in good accordance with the structure design. Fig. 6(c) presents a metallographic micrograph of a physical PIN structure back-illuminated AlGa_{0.4}N-based SUV-PD. The detailed fabrication process is also described in the experimental section above. The dark current–voltage (I - V) characteristics are shown in Fig. 6(d) on both linear and semi-log scales. It can be seen that the dark I - V characteristics show good rectifying behavior, with a current density of 5.56×10^{-7} A mm⁻² under a 10 V reverse bias. The spectral responsivity and corresponding EQE under

zero-bias are also measured, as shown in Fig. 6(e). As can be seen, the response spectrum presents bandpass response characteristics ranging from 262 nm to 282 nm, with a peak value of 0.15 A W⁻¹ at 271 nm, corresponding to a high EQE of 68.8%. The ultraviolet/visible rejection ratio is more than four orders of magnitude. In order to evaluate the response speed of the device, a transient spectral response at zero-bias is stimulated *via* a 266 nm-wavelength pulsed Nd:YAG laser with a pulse width of 10 ns, which is recorded using a Tektronix DPO 5104 digital oscilloscope. As shown in Fig. 6(f), a response time (τ_{rise}) of 6.5 ns is presented, which is defined as the rise time for the response current to increase from 10% to 90% of the peak value, and a decay section. The decay section is well fitted by a first-order double exponential decay function containing a fast decay component ($\tau_1 = 67$ ns) and a slow one ($\tau_2 = 0.95$ μ s). The good performance of the PIN structure back-illuminated AlGa_{0.4}N-based SUV-PD can be attributed to the optimized quality of the AlN template grown *via* a combination of a two-step growth method and a MT-AlN interlayer.

4. Conclusions

In summary, the influence of different MT-AlN interlayer cycles on the crystalline quality of AlN templates is demonstrated in

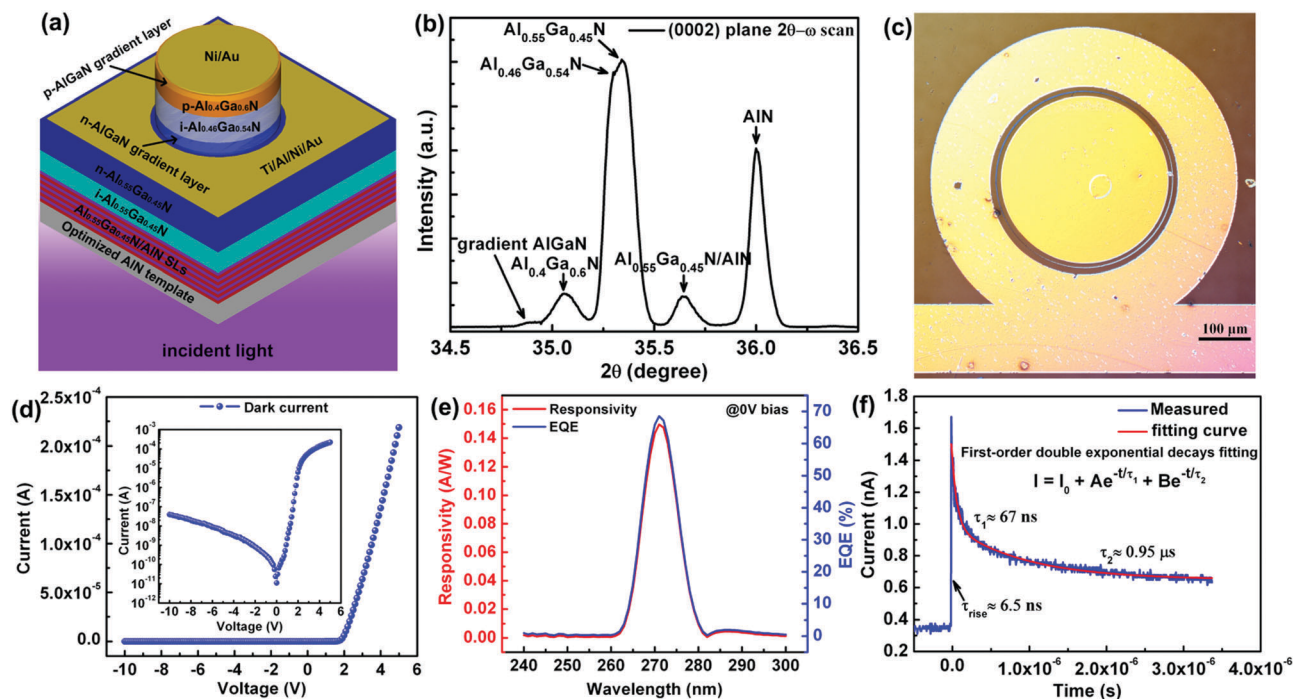


Fig. 6 The performance of the back-illuminated AlGaIn-based SUV-PD based on an optimized AlN template. (a) A schematic diagram of the configuration of the PIN structure back-illuminated AlGaIn-based SUV-PD. (b) $2\theta - \omega$ scan results from the (0002) plane for the epitaxial material via HRXRD. (c) A metallographic micrograph of a physical AlGaIn-based SUV-PD. (d) An $I-V$ curve of the back-illuminated PIN structure AlGaIn-based SUV-PD in a dark environment. The inset presents the $I-V$ curve on a semi-log scale. (e) The spectral responsivity and EQE of the back-illuminated PIN structure AlGaIn-based SUV-PD under zero-bias. (f) The decay edge of the transient spectral response under zero-bias.

this paper. The results reveal that the crystalline quality, surface morphology and residual compressive stress of an AlN template can be greatly improved by introducing a MT-AlN interlayer during the growth of HT-AlN, in comparison with a common growth method. And the optimized growth of the AlN template can be obtained by inserting one MT-AlN interlayer cycle. The MT-AlN interlayer plays the role of a strain gradient to release residual compressive stress in AlN via elongation along the direction perpendicular to the sample surface. Based on the optimized AlN template, a PIN structure back-illuminated AlGaIn-based SUV-PD is further designed, grown and fabricated. The performance of the SUV-PD is carefully evaluated and the results show that the device exhibits a low dark current density, a bandpass spectral responsivity in the solar-blind ultraviolet band with a peak value of 0.15 A W^{-1} at 271 nm, corresponding to an EQE as high as 68.8%, and a response speed of 6.5 ns. These results strongly reflect the quality of the AlN template.

Conflicts of interest

There are no conflicts of interest to declare.

Acknowledgements

This work was partially supported by the National Natural Science Foundation of China (Grant No. 61504144 and 51472230), and the Jilin Provincial Science & Technology Department (Grant No. 20170520156JH).

References

- 1 E. Matioli, S. Brinkley, K. M. Kelchner, Y.-L. Hu, S. Nakamura, S. DenBaars, J. Speck and C. Weisbuch, *Light: Sci. Appl.*, 2012, **1**, e22.
- 2 Y. Lin, S. Zhou, W. Wang, W. Yang, H. Qian, H. Wang, Z. Lin, Z. Liu, Y. Zhu and G. Li, *J. Mater. Chem. C*, 2015, **3**, 1484–1490.
- 3 J. Yan, J. Wang, Y. Zhang, P. Cong, L. Sun, Y. Tian, C. Zhao and J. Li, *J. Cryst. Growth*, 2015, **414**, 254–257.
- 4 S. Zhao, X. Liu, S. Y. Woo, J. Kang, G. A. Botton and Z. Mi, *Appl. Phys. Lett.*, 2015, **107**, 043101.
- 5 H. Taketomi, Y. Aoki, Y. Takagi, A. Sugiyama, M. Kuwabara and H. Yoshida, *Jpn. J. Appl. Phys.*, 2016, **55**, 05FJ05.
- 6 H.-F. Chen, Y.-R. Chen, H. Song, Z.-M. Li, H. Jiang, D.-B. Li, G.-Q. Miao, X.-J. Sun and Z.-W. Zhang, *Phys. Status Solidi A*, 2017, **214**, 1600932.
- 7 E. Cicek, R. McClintock, Z. Vashaei, Y. Zhang, S. Gautier, C. Y. Cho and M. Razeghi, *Appl. Phys. Lett.*, 2015, **102**, 051102.
- 8 Z. Bryan, I. Bryan, J. Xie, S. Mita, Z. Sitar and R. Collazo, *Appl. Phys. Lett.*, 2015, **106**, 142107.
- 9 Y. Chen, H. Song, D. Li, X. Sun, H. Jiang, Z. Li, G. Miao, Z. Zhang and Y. Zhou, *Mater. Lett.*, 2014, **114**, 26–28.
- 10 Y. Kangawa, R. Toki, T. Yayama, B. M. Epelbaum and K. Kakimoto, *Appl. Phys. Express*, 2011, **4**, 095501.
- 11 A. Shatskiy, Y. M. Borzdov, D. Yamazaki, K. D. Litasov, T. Katsura and Y. N. Palyanov, *Cryst. Growth Des.*, 2010, **10**, 2563–2570.

- 12 C. Hartmann, J. Wollweber, C. Seitz, M. Albrecht and R. Fornari, *J. Cryst. Growth*, 2008, **310**, 930–934.
- 13 P. Dong, J. Yan, J. Wang, Y. Zhang, C. Geng, T. Wei, P. Cong, Y. Zhang, J. Zeng, Y. Tian, L. Sun, Q. Yan, J. Li, S. Fan and Z. Qin, *Appl. Phys. Lett.*, 2013, **102**, 241113.
- 14 M. Moseley, A. Allerman, M. Crawford, J. J. Wierer Jr., M. Smith and L. Biedermann, *J. Appl. Phys.*, 2014, **116**, 053104.
- 15 H. Liu, G. Chen, Y. Lan, G. Lee and J. Chyi, *Proc. SPIE*, 2009, **7216**, 72160I.
- 16 T. Y. Wang, J. H. Liang, G. W. Fu and D. S. Wu, *CrystEngComm*, 2016, **18**, 9152–9159.
- 17 M. Conroy, V. Z. Zubialeovich, H. Li, N. Petkov, J. D. Holmes and P. J. Parbrook, *J. Mater. Chem. C*, 2015, **3**, 431–437.
- 18 J. Kim, J. Pyeon, M. Jeon and O. Nam, *Jpn. J. Appl. Phys.*, 2015, **54**, 081001.
- 19 R. G. Banal, Y. Akashi, K. Matsuda, Y. Hayashi, M. Funato and Y. Kawakami, *Jpn. J. Appl. Phys.*, 2013, **52**, 08JB21.
- 20 L. W. Sang, Z. X. Qin, H. Fang, T. Dai, Z. J. Yang, B. Shen, G. Y. Zhang, X. P. Zhang, J. Xu and D. P. Yu, *Appl. Phys. Lett.*, 2008, **93**, 122104.
- 21 H. Miyake, C. Lin, K. Tokoro and K. Hiramatsu, *J. Cryst. Growth*, 2016, **456**, 155–159.
- 22 H. Fukuyama, H. Miyake, G. Nishio, S. Suzuki and K. Hiramatsu, *Jpn. J. Appl. Phys.*, 2016, **55**, 05FL02.
- 23 Y. Chen, Z. Zhang, Z. Li, H. Jiang, G. Miao and H. Song, *Phys. Status Solidi A*, 2018, **215**, 1700358.
- 24 X. Sun, D. Li, Y. Chen, H. Song, H. Jiang, Z. Li, G. Miao and Z. Zhang, *CrystEngComm*, 2013, **15**, 6066–6073.
- 25 M. Takeuchi, H. Shimizu, R. Kajitani, K. Kawasaki, T. Kinoshita, K. Takada, H. Murakami, Y. Kumagai, A. Koukitu, T. Koyama, S. F. Chichibu and Y. Aoyagi, *J. Cryst. Growth*, 2007, **305**, 360–365.
- 26 H. Jiang, T. Egawa, M. Hao and Y. Liu, *Appl. Phys. Lett.*, 2005, **87**, 241911.
- 27 W. Wang, H. Yang and G. Li, *J. Mater. Chem. C*, 2013, **1**, 4070–4077.
- 28 S. R. Lee, A. M. West, A. A. Allerman, K. E. Waldrup, D. M. Follstaedt, P. P. Provencio and D. D. Koleske, *Appl. Phys. Lett.*, 2005, **86**, 241904.
- 29 T. Prokofyeva, M. Seon, J. Vanbuskirk and M. Holtz, *Phys. Rev. B: Condens. Matter Mater. Phys.*, 2001, **63**, 125313.
- 30 M. Balaji, A. Claudel, V. Fellmann, I. Gélard, E. Blanquet, R. Boichot, A. Pierret, B. Attal-Trétout, A. Crisci, S. Coindeau, H. Roussel, D. Pique, K. Baskar and M. Pons, *J. Alloys Compd.*, 2012, **526**, 103–109.
- 31 S. Yang, R. Miyagawa, H. Miyake, K. Hiramatsu and H. Harima, *Appl. Phys. Express*, 2011, **4**, 031001.
- 32 V. Yu. Davydov, Yu. E. Kitaev, I. N. Goncharuk, A. N. Smirnov, J. Graul, O. Semchinova, D. Uffmann, M. B. Smirnov, A. P. Mirgorodsky and R. A. Evarestov, *Phys. Rev. B: Condens. Matter Mater. Phys.*, 1998, **58**, 12899–12907.
- 33 A. Kadir, C. C. Huang, K. E. K. Lee, E. A. Fitzgerald and S. J. Chua, *Appl. Phys. Lett.*, 2014, **105**, 232113.
- 34 V. Darakchieva, J. Birch, M. Schubert, T. Paskova, S. Tungasmita, G. Wagner, A. Kasic and B. Monemar, *Phys. Rev. B: Condens. Matter Mater. Phys.*, 2004, **70**, 045411.